

GRP78-targeted and doxorubicin-loaded nanodroplets combined with ultrasound: a potential novel theranostics for castration-resistant prostate cancer

Yading Zhao , Dandan Shi, Mengmeng Shang, Xiao Sun, Lu Guo, Dong Meng, Xinxin Liu, Xiaoying Zhou  and Jie Li

Department of Ultrasound, Qilu Hospital of Shandong University, Jinan, China

ABSTRACT

The construction of multifunctional oncotherapy nanoplatfoms that combine diagnosis and treatment remains challenging. Nanodroplets (NDs), which simultaneously enhance ultrasound imaging and therapeutic effects, are a potential strategy for non-invasive drug delivery. To achieve the goals of precise medicine, novel SP94 peptide-modified and doxorubicin-loaded ultrasonic NDs (SP94-DOX-NDs) for castration-resistant prostate cancer (CRPC) targeting and treatment were constructed in this study. The characteristics, contrast-enhanced ultrasound imaging (CEUI), targeting ability to glucose-regulated protein 78 (GRP78)-overexpressing CRPC and anticancer effect of the SP94-DOX-NDs were assessed. The desired SP94-NDs were successfully prepared using the nanoemulsification method using a certain proportion of SP94-PEG-chitosan, perfluoropentane (PFP), Tween 20, and lecithin. SP94-NDs with a size of ~300 nm showed great biocompatibility and CEUI ability. Compared with blank NDs, SP94-NDs exhibited higher tumor-specific targeting ability due to conjugation between the SP94 peptide and GRP78-overexpressing 22RV1 cells. Most importantly, *in vitro* and *in vivo* investigations showed that SP94-DOX-NDs combined with ultrasound could specifically deliver DOX into 22RV1 cells and thereby demonstrated a stronger anticancer effect than DOX-NDs and DOX. Thus, SP94-DOX-NDs may provide an efficient approach for the real-time imaging of tumors and triggered, accurate drug delivery to tumors.

ARTICLE HISTORY

Received 27 October 2021
Revised 19 December 2021
Accepted 20 December 2021

KEYWORDS

Nanodroplets; glucose-regulated protein 78; ultrasound imaging; theranostics; castration-resistant prostate cancer

1. Introduction

Prostate cancer (PCa), the second most common malignant tumor in men that is only surpassed by lung cancer, has attracted growing attention worldwide (Bray et al., 2018). As the cornerstone treatment for PCa, androgen deprivation therapy has a limited duration, and most patients tend to develop castration-resistant prostate cancer (CRPC). Chemotherapy is currently the primary method for treating CRPC. However, the effective drug concentration at a tumor site is not sufficiently high, and the side effects of systemic administration are considerable, thereby affecting the prognosis of CRPC. A targeted drug delivery system (TDDS) may provide a solution (Cai et al., 2012; Du et al., 2012; Li et al., 2015; Yang et al., 2015). Compared with other TDDSs, ultrasonic nanodroplets (NDs) can promote safe and highly efficient drug delivery and advance the accurate and visual diagnosis and treatment of cancer. NDs with liquid cores overcome the shortcomings of traditional ultrasound contrast agents with gaseous cores, which are relatively large in diameter and not sufficiently stable in blood circulation (Li et al., 2020). The small size of NDs allows them to reach a tumor site through an enhanced permeability and retention (EPR)

effect. Once exposed to ultrasound, the droplets are transformed into bubbles *via* acoustic droplet vaporization (ADV), enhancing tissue contrast (Kripfgans et al., 2004). Additionally, sonoporation occurs, generating holes in the adjoining cell membrane and thus enhancing cellular permeability. The NDs are then destroyed, causing the drug to be locally released at the tumor site, which results in successful maximization of their antitumor effects and minimization of their side effects (Duan et al., 2017; Lv et al., 2017). Compared with other DDSs, ultrasonic NDs are particularly attractive because they can determine when and where to release the encapsulated drugs through ultrasound sonoporation, thereby effectively contributing to tumor treatment.

Glucose-regulated protein 78 (GRP78) can regulate the unfolded protein response (UPR) process and is mainly in the endoplasmic reticulum (ER) (Lee, 2007). Under stress conditions, such as glucose deficiency or hypoxia, the accumulation of misfolded and underglycosylated proteins can induce the UPR, which allows GRP78 to translocate to the membrane of cancer cells (Lee, 2007; Zhang et al., 2010). GRP78 is, therefore, an effective target for cancer treatment (Lee, 2014). GRP78 is overexpressed on the PCa cell membrane, and the SP94 peptide can specifically bind to GRP78

(Pootrakul et al., 2006; Delie et al., 2013; Jiang et al., 2019). The SP94 peptide has outstanding advantages, such as small size, little immunogenicity, and economic synthesis (Schottelius & Wester, 2009); offers an ideal ligand for targeting CRPC; and binds to the target by connecting to ultrasonic NDs.

However, no studies have investigated GRP78-targeted and ultrasound-responsive NDs in CRPC therapy. Thus, we prepared SP94-modified ultrasonic NDs for the encapsulation of doxorubicin (DOX) and PFP, verified the targeting ability of the SP94-DOX-NDs on CRPC, and investigated the inhibitory effect of SP94-DOX-NDs combined with ultrasound on the growth of CRPC.

2. Materials and methods

2.1. Materials

SFSIIHTPILPLGGC peptide (SP94) and MAL-PEG2000-NHS were supplied by Ruixi Company (Xian, China). PFP was supplied by J&K Scientific Ltd. (Beijing, China). Chitosan (CS; MW 5.0 kDa, degree of deacetylation 90%) was supplied by Sigma-Aldrich (MO, USA). Dil was supplied by Beyotime (Haimen, China). Tween 20, lecithin, and DOX were supplied by Solarbio (Beijing, China). Anti-GRP78 antibodies and anti-KI67 antibodies were supplied by Proteintech Company (Wuhan, China). 4-Phenylbutyric acid (4-PBA) was supplied by Macklin Biochemical (Shanghai, China), and DyLight 488 and goat anti-rabbit IgG were purchased from Abbkine Scientific Company (Wuhan, China). RPMI 1640 medium, DMEM, 0.25% trypsin-EDTA, fetal bovine serum (FBS), and antibiotics (penicillin 100 U/mL and streptomycin 100 mg/mL) were purchased from Gibco Company (NY, USA).

2.2. Cell lines

The human CRPC cell line 22RV1 was obtained from Qilu Hospital of Shandong University (Shandong, China), and the human prostate stromal cell line WPMY-1 was purchased from the Type Culture Collection of the Chinese Academy of Sciences (Shanghai, China). 22RV1 and WPMY-1 cells were grown in RPMI 1640 and DMEM supplemented with FBS and antibiotics, respectively.

2.3. Synthesis and identification of SP94-PEG2000-CS

SP94-PEG2000-CS was synthesized by covalently coupling SP94-SH with CS-PEG2000-MAL *via* a sulfhydryl-maleimide coupling reaction, which is described briefly as follows. To obtain CS-PEG2000-MAL, 50 mg of chitosan was dissolved in 10 mL of deionized water; MAL-PEG2000-NHS (1.0 eq.) was added to the chitosan solution, and the mixture was then stirred for 24 h using a thermostatic magnetic stirrer at room temperature. Thereafter, anhydrous DMF containing SP94 (2 mL, 1.0 eq.) was slowly added and stirred for 24 h. Next, the mixture was dialyzed (molecular weight cutoff = 3500 Da) against deionized water for 48 h. The solution was then lyophilized for further use. The composition of the

conjugated compound was ascertained by ¹HNMR spectroscopy (AVANCE III HD 400, Bruker, Germany).

2.4. Preparation and characterization of the nanodroplets

Nanodroplets were successfully created *via* the nanoemulsion method described in the literature (Baghbani et al., 2016). First, PFP, lecithin, and Tween 20 with or without DOX were added to deionized water and homogenized (FJ2000-S homogenizer, China) for 1 min at 20,000 rpm under ice bath conditions. Next, SP94-PEG2000-CS solution (2% w/v) was added, and the solution was homogenized for another 2 min. After centrifugation at 300 rpm for 5 min, the upper layer of the solution was acquired and filtered through a 0.45- μ m filter. The obtained SP94-NDs or SP94-DOX-NDs were washed with PBS three times to remove the impurities and free DOX. The purified SP94-NDs or SP94-DOX-NDs were resuspended in sterile PBS and stored at 4 °C for further use.

Under transmission electron microscopy (TEM) (JEOL, Tokyo, Japan), the morphology of the SP94-NDs and SP94-DOX-NDs was observed. The particle size and zeta potential of the SP94-NDs and SP94-DOX-NDs were detected using a Delsa Nano C Analyzer (Beckman Coulter, USA). In addition, the serum stability of SP94-NDs and SP94-DOX-NDs was evaluated by detecting the change in particle size at different moments in 10% FBS. The ultrasound-responsive drug release profile of the SP94-DOX-NDs was evaluated by the dialysis method. One milliliter of the SP94-DOX-NDs solution was placed in a dialysis sack (molecular weight cutoff 3500, Sigma, MO, USA) and immersed in 8 mL of PBS. The SP94-DOX-NDs were sonicated by ultrasound (WED-100 ultrasonic therapy equipment, Honda Hi-Tech, Shenzhen, China) for 0, 1, 2, 4, 6, and 8 min with 0.5 W/cm². At each time interval, 1 mL of solution was removed, and 1 mL of fresh PBS was added. The amount of DOX released was measured by a UV-Vis spectrophotometer. Accumulative release of DOX (%) = the amount of DOX released/the amount of DOX initially encapsulated in SP94-DOX-NDs \times 100%.

2.5. Cytotoxicity

22RV1 cells were seeded in a 96-well plate at a density of 2×10^4 cells/well and allowed to grow overnight. After treatment with RPMI 1640 containing nanodroplets at different concentrations for 24 h, the cells were incubated with CCK-8. The absorbance was measured with a microplate reader (UV-2450, SHIMADZU, Tokyo, Japan).

2.6. Hemolysis

The experiment was approved by the Research Ethics Committee of Qilu Hospital of Shandong University. Hemolysis is an important indicator of material safety, and quantitatively measures the leakage of hemoglobin from erythrocytes (Lekshmi et al., 2011). Written informed consent of the participant was acquired. Four milliliters of anticoagulated blood from the remainder of the analytical blood with

normal values were taken and diluted in sterile 0.9% saline. Whole blood dilutions were centrifuged at 1500 rpm for 10 min. Nanodroplets at different concentrations, 0.9% saline (negative control, 0% hemolysis) and deionized water (positive control, 100% hemolysis) were mixed with the obtained blood cell suspension for 1 h at 37 °C, and the mixtures were centrifuged at 1200 rpm for 5 min. The supernatant was detected at a wavelength of 545 nm using a microplate reader. The hemolytic rate was determined based on the following formula:

$$\text{Hemolytic Rate (\%)} = (\text{OD}_{\text{sample}} - \text{OD}_{\text{negative}}) / (\text{OD}_{\text{positive}} - \text{OD}_{\text{negative}}) \times 100\%$$

2.7. In vitro CEUI

To realize CEUI, a 9-L probe of an ultrasound scanning system (LOGIQ E9; GE, USA) was used. SP94-NDs or PBS (control) was placed into the tube cut off from a pipette. Next, the tube was fixed in degassed water at 37 °C. During ultrasound imaging, the center frequency was 9.0 MHz, the transmit power was 70%, and the dynamic range was 60 dB. Using the 'TIC analysis' function of the device, the CEUI capability was determined by the relative intensity, which was obtained by subtracting the contrast intensity of the background from that of the region of interest (ROI). Then relative intensities were used to draw the time-intensity curve.

2.8. Distribution of GRP78 protein in CRPC cell lines 22RV1

22RV1 cells and WPMY-1 cells were seeded into a 24-well plate covered with glass slides at a density of 4×10^4 cells/well and placed in an incubator overnight. The cells were exposed to anti-GRP78 antibody overnight at 4 °C. After incubation with DyLight 488-labeled secondary antibodies, the cells were observed *via* fluorescence microscopy (OLYMPUS BX41, Olympus Corporation, Tokyo, Japan).

2.9. In vitro targeted binding ability

Dil was used as a fluorescent probe to explore the cell-targeting ability of nanodroplets. After adding a small amount of Dil, the nanodroplets were ultracentrifuged to obtain Dil-labeled nanodroplets. WPMY-1 and 22RV1 cells were seeded in 6-well plates (2×10^5 cells/well) and incubated with a culture medium containing Dil-labeled targeted SP94-NDs or non-targeted NDs for 2 h. The cell-targeting ability of nanodroplets was evaluated by fluorescence microscopy and flow cytometry (FCM).

According to the literature (Chen et al., 2019; Jiang et al., 2020), 4-PBA is an ER stress inhibitor that inhibits the UPR. The commonly used blocking dose ranged from 0.5 to 10 mM. According to the results of preliminary experiments, 5 mM 4-PBA was selected. To confirm that the cell-targeting ability of SP94-NDs may be mediated by GRP78, we exposed 22RV1 cells to the ER stress inhibitor 4-PBA for 2 h, and the

cell-targeting ability of SP94-NDs was then observed by fluorescence microscopy.

2.10. Optimization of DOX-loaded nanodroplets

To prevent DOX photolysis, all operations with DOX were protected from light. DOX-loaded nanodroplets were constructed at different initial doses to determine the optimal encapsulation efficiency (EE) and loading efficiency (LE). After the nanodroplets were centrifuged at 12,000 rpm for 15 min, the DOX content in the supernatant was detected at a wavelength of 480 nm using a UV-Vis spectrophotometer (Thermo Fisher, USA). The EE and LE were calculated with the following equations:

$$\text{EE} = (A - B) / A \times 100\%$$

$$\text{LE} = (A - B) / (A + C) \times 100\%$$

where A is the total amount of DOX given, B is the amount of DOX in the supernatant (free DOX), and C is the total amount of SP94-CS given.

2.11. Increased intracellular uptake of DOX by SP94-DOX-NDs under ultrasound irradiation

Because SP94-DOX-NDs are desired to deliver more DOX to tumor cells, the intracellular uptake of DOX must be determined, and this is accomplished using ultrasound irradiation. Considering cytotoxicity, the 50% inhibition concentration (IC50) of DOX was calculated. Ultrasound stimulation was performed using a therapeutic ultrasound device (WED-100, Honda Hi-Tech, Shenzhen, China), and the parameters were set as follows: fixed-frequency = 1 MHz, duty cycle = 70%, pulse repetition rate = 100 Hz, sound intensity = 0.5 W/cm², and time = 60 s (Meng et al., 2019). Cells were exposed for 2 h to different treatments (PBS, DOX, DOX-NDs, SP94-DOX-NDs) with and without ultrasound irradiation while maintaining the DOX concentration of the different groups at the same level. After fixation with 4% paraformaldehyde, cells were examined *via* fluorescence microscopy.

2.12. In vitro antitumor effect

22RV1 cells were seeded into 96-well plates at a density of 4×10^4 cells/well. The cells were then exposed to different treatments (PBS, DOX, DOX-NDs, and SP94-DOX-NDs) with and without ultrasound irradiation for 24 h while maintaining the DOX concentration of the different groups at the same level. The absorbance was detected using a microplate reader.

2.13. Animal xenograft model

Animal experiments were approved by the Research Ethics Committee of Qilu Hospital of Shandong University. In a humidity- and temperature-controlled environment, thirty male BALB/c nude mice (4–6 weeks old, ~15 g, Beijing Weitonglihua Co., Beijing, China) were kept in a cabinet with laminar air flow under pathogen-free conditions. To form

xenograft tumors, the mice were inoculated in the right back with 3×10^6 22RV1 cells in 100 μ L of PBS.

2.14. In vivo targeted binding ability

When the tumor volume reached $\sim 300 \text{ mm}^2$, nude mice were randomly divided into two groups with five mice per group. The mice were administered 100 μ L of Dil-labeled NDs or SP94-NDs (Dil: 0.25 mg/kg) *via* the tail vein. All mice were placed in a darkroom (IVIS Spectrum, PerkinElmer, USA) to detect Dil fluorescence (excitation filter: 549 nm, emission filter: 565 nm) after ~ 2 h. The fluorescence intensity was quantified by the average radiance of the ROI of the tumor site.

2.15. The biodistribution of SP94-DOX-NDs *ex vivo*

The tumor-carrying nude mice were sacrificed at different time intervals after the injection of SP94-DOX-NDs solution (4 mg/kg DOX, 100 μ L per mouse) *via* the tail vein. Major organs and tumors were harvested for fluorescence imaging and quantification using the IVIS spectrum imaging system (PerkinElmer, Waltham, MA, USA). To detect the DOX fluorescence, the excitation filter was 480 nm, and the emission filter was 580 nm. The fluorescence intensity was quantified by the average radiance of the ROI.

2.16. In vivo CEUI

When the tumor volume reached $\sim 100 \text{ mm}^3$, SP94-NDs (4 mg/mL, 200 μ L) were injected into the tail vein of mice. CEUI images were collected immediately post-injection using an ultrasound diagnostic apparatus (LOGIQ E9; GE, USA, 9.0 MHz center frequency; 0.14 mechanical index (MI); 60 dB dynamic range).

2.17. In vivo biosafety

Mice were injected with SP94-NDs (4 mg/mL, 200 μ L per mouse) or saline (200 μ L per mouse) and randomly allocated to two groups. On the 7th day, major organs and blood samples were acquired. Blood samples were analyzed based on different indicators, including blood urea nitrogen (BUN), alanine aminotransferase (ALT), creatinine (CRE), and albumin (ALB). The hematoxylin and eosin (HE) staining of major organs (heart, liver, spleen, lung, and kidney) was analyzed.

2.18. In vivo antitumor effect

When the tumors reached $\sim 100 \text{ mm}^3$ in size, nude mice were randomly divided into six groups and received different treatments on days 3, 6, 9, and 12 once per day. Each group received different treatments as follows: control (PBS, 100 μ L); DOX (4 mg/kg, 100 μ L); DOX + US (4 mg/kg, 100 μ L, ultrasound irradiation at 2 h after the injection of DOX *via* the tail vein); DOX-NDs + US (100 μ L, ultrasound irradiation at 2 h after the injection of DOX-NDs *via* the tail vein); SP94-DOX-NDs + US (100 μ L, ultrasound irradiation at 2 h after the

injection of SP94-DOX-NDs *via* the tail vein); and SP94-DOX-NDs (100 μ L). The concentration of DOX wrapped in the nanodroplets was equivalent to 4 mg/kg DOX. The ultrasound parameters were set as follows: fixed-frequency = 1 MHz, duty cycle = 70%, pulse repetition rate = 100 Hz, sound intensity = 1.5 W/cm², and irradiation time = 60 s. Tumor volumes and body weights were recorded every 2 days, and the tumor volume was calculated using the following equation:

$$\text{Tumor volume (mm}^3\text{)} = 1/2 \times \text{length} \times \text{width}^2.$$

On the 14th day, the tumors were excised and stained with HE to detect tissue damage, TUNEL to detect cell apoptosis or Ki-67 to detect cell proliferation. Ki-67 positive index was measured by quantifying brown areas (cell nuclei) using ImageJ software.

2.19. Statistical analysis

All experiments were performed in triplicate. The results are shown as the means \pm SD and were analyzed statistically by a *t*-test or one-way ANOVA using SPSS software (version 19.0, USA). Double asterisks indicate that $p < .01$ and that the result is statistically significant.

3. Results

3.1. Characterization of SP94-PEG2000-CS, SP94-NDs, and SP94-DOX-NDs

SP94-PEG2000-CS was synthesized according to the scheme shown in Figure 1(A). The chemical structure of the obtained SP94-PEG2000-CS was characterized *via* the ¹HNMR spectrum shown in Figure 1(B), where the presence of characteristic signals of each moiety (at 7.15–7.26 ppm for SP94; at 3.05 ppm for CS; and at 3.60 ppm for PEG2000) indicated their identities. Compared with CS, the ¹HNMR spectrum of SP94-PEG2000-CS showed signals of multiple peaks within 7.15–7.26 ppm, which were attributed to the SP94 peptide. According to the integration of the characteristic peaks, the molar ratio of CS, PEG2000, and SP94 was 1:1:1. The content of conjugated SP94 and PEG2000 is about 18.2 and 23.4%. This information verified that the required SP94-PEG2000-CS was synthesized successfully.

As shown in Figure 1(C), the particle size of SP94-NDs was 299.7 nm, and the zeta potential was +14.94 mV. After loading with DOX, the mean diameter of SP94-DOX-NDs was 291.8 ± 33.1 nm, and the zeta potential was $+10.7 \pm 0.8$ mV (Figure 1(F)). The TEM images illustrated that the SP94-NDs and SP94-DOX-NDs exhibited uniform spheroids (Figures 1(D,E)). The serum stability of SP94-NDs and SP94-DOX-NDs was also evaluated. As observed in Figure 1(G), the particle size of them in 10% FBS did not change significantly over 36 h, further indicating that nanodroplets could resist serum-induced aggregation and remain stable in circulation for application as DDSs. In addition, the effect of ultrasound exposure on the DOX release was investigated. The cumulative amount of DOX released from SP94-DOX-NDs was only

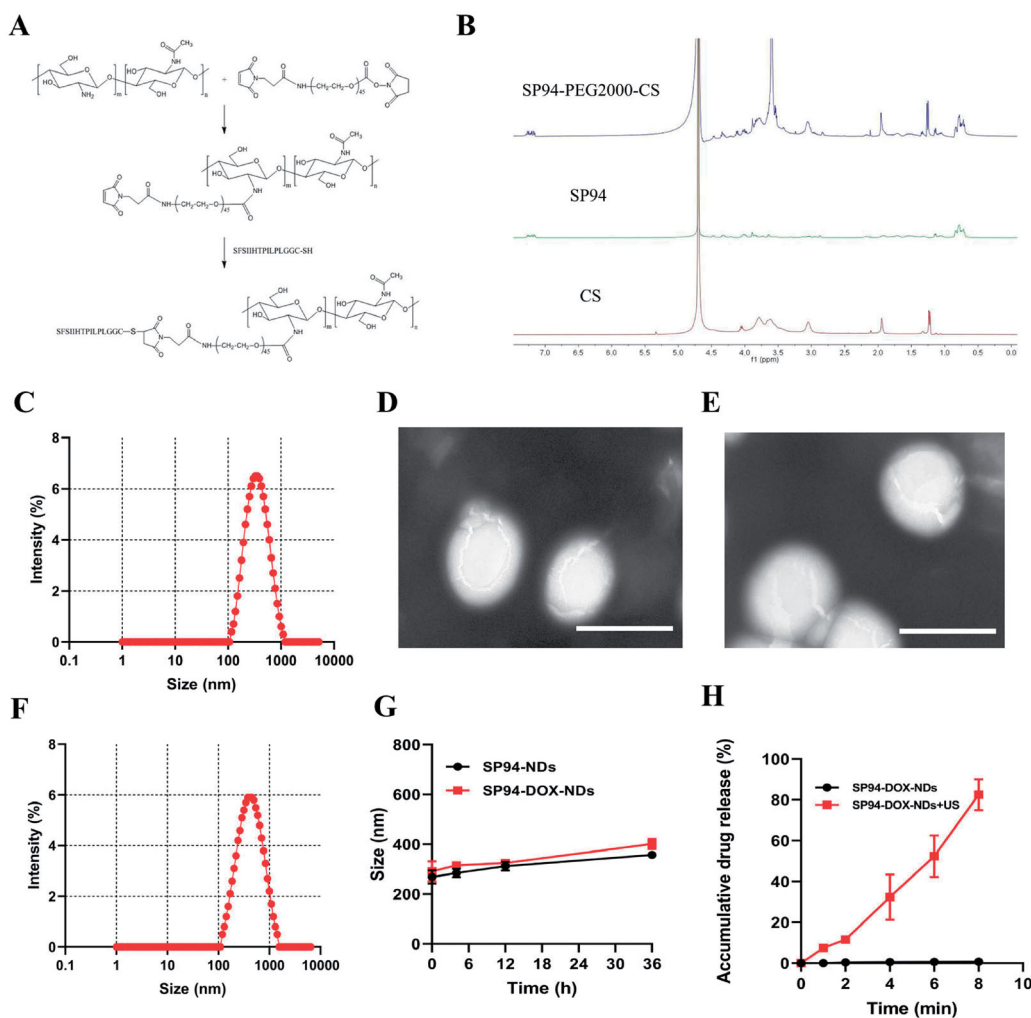


Figure 1. Characterization of SP94-PEG2000-CS, SP94-NDs, and SP94-DOX-NDs. (A) Synthetic scheme of SP94-PEG2000-CS. (B) ^1H NMR spectra of SP94-PEG2000-CS. SP94: SFSIIHTPLPLGGC; CS: Chitosan. (C) Particle size of SP94-NDs. (D) TEM image of SP94-NDs. Scale bar: 500 nm. (E) TEM image of SP94-DOX-NDs. Scale bar: 500 nm. (F) Particle size of SP94-DOX-NDs. (G) Serum stability of SP94-NDs and SP94-DOX-NDs. (H) Drug release profile of SP94-DOX-NDs under US irradiation. Data are expressed as means \pm SD ($n = 3$).

0.71 \pm 0.27% within 8 min (Figure 1(H)). With ultrasound exposure for 8 min, a massive amount (82.53 \pm 6.18%) of DOX was released from the nanodroplets, which indicated that the US mediated the 'drug dumping' effect.

3.2. Biosafety and biodistribution

The following experiments were carried out to confirm the biosafety of nanodroplets. In the cytotoxicity assay, the cell viability of nanodroplets at different concentrations was above 80% (Figure 2(A)). In the hemolysis assay, Figure 2(B) showed that even though the concentration of nanodroplets was 800 $\mu\text{g}/\text{mL}$, the hemolytic rate was <2%. As shown in Figures 2(C,D), the biochemical parameters investigated in this study were within the reference range of normal values in both groups. HE staining of major organs revealed no evident abnormalities, including inflammation, cell necrosis, and apoptosis, in the SP94-NDs and the control (saline) groups, indicating that SP94-NDs had no toxicity to nude mice at the tested doses.

The biodistribution of SP94-DOX-NDs in nude mice at different time intervals was also investigated. As shown in

Figure 2(E), the fluorescent signal was mainly concentrated in tumor tissue, indicating that the SP94-DOX-NDs could selectively and efficiently accumulate in tumors, which may be related to the active targeting effect of the SP94 peptide. Even after 24 h, the fluorescent signal was retained in the tumor tissue, indicating the long retention of SP94-DOX-NDs at the tumor site. The fluorescence signal of the tumor and other organs were quantified by calculating the average radiant efficiency (Figure 2(F)). SP94-DOX-NDs have a long intratumoral retention time and the highest tumor accumulation at 2 h after injection. Therefore, we performed US irradiation on the tumors of nude mice 2 h post-administration in subsequent experiments. Furthermore, in addition to targeting tumors, signals were detected in the liver and kidneys.

3.3. Targeted binding ability

DDSs modified by ligands could bind to specific receptors on cancer cell membranes, which could accurately deliver drugs to the desired sites, also known as 'active targeting'. First, we conducted an immunofluorescence assay to compare GRP78 expression in non-cancerous (WPMY-1) and cancerous

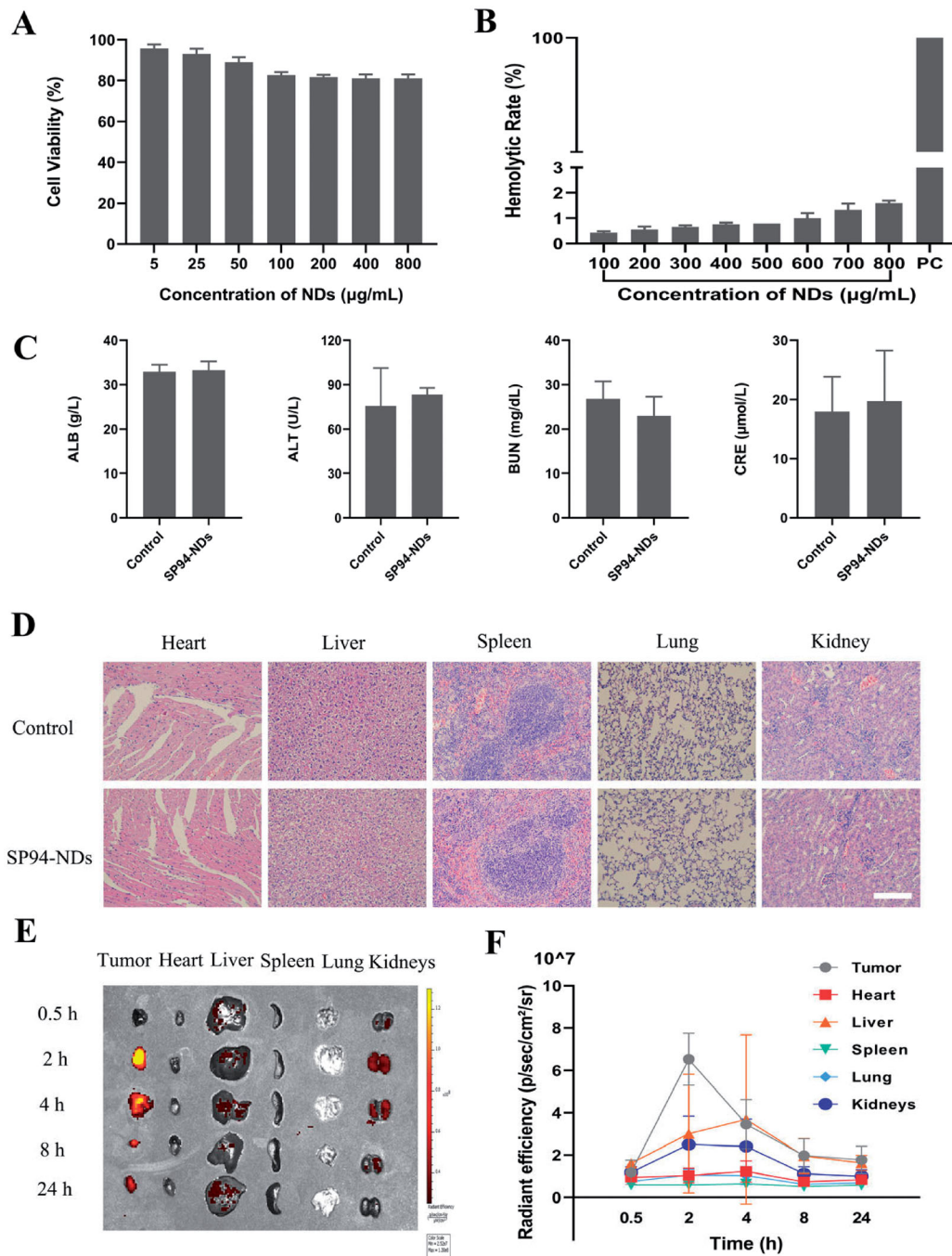


Figure 2. Biosafety and Biodistribution. (A) Cell viability comparison between different concentrations of nanodroplets. (B) Hemolytic rate at different concentrations of nanodroplets and deionized water (positive control, PC). (C) Biochemical parameters in different groups. (D) HE staining of major organs in different groups. Scale bar: 50 µm. (E) Biodistribution of SP94-DOX-NDs in nude mice at different time intervals *ex vivo*. (F) Quantitative analysis of average radiation efficiency in the harvested organs and tumors from (E). Data are expressed as means \pm SD ($n = 3$).

(22RV1) cell lines. As shown in Figure 3(A), GRP78 showed high expression on the cell membrane of 22RV1 cells, with green fluorescence attached to the cell surface, and showed low expression on the WPMY-1 cell membrane, with no marked green fluorescence on the cell surface. The results indicated that 22RV1 cells exhibited significantly higher GRP78 expression than WPMY-1 cells. Next, the targeted binding ability of SP94-NDs and NDs *in vitro* was investigated using fluorescence microscopy and FCM (Figures 3(B,C)). In the targeted SP94-NDs group, many SP94-NDs aggregated and surrounded 22RV1 cells, but much fewer SP94-NDs were

observed in WPMY-1 cells. In the non-targeted NDs group, no marked NDs aggregation was found on either 22RV1 or WPMY-1 cells. FCM data further confirmed the results of fluorescence microscopy imaging (Figure 3(E)). The aggregation of 22RV1 cells in the SP94-NDs group was greater than that in the NDs group (21.80 ± 0.30 vs. $2.09 \pm 0.35\%$, $p < .01$). The SP94-NDs group had a lower targeting ability to WPMY-1 cells than to 22RV1 cells (6.43 ± 0.69 vs. $21.80 \pm 0.30\%$, $p < .01$). For non-targeted NDs, a low cell internalization rate was found with both 22RV1 cells and WPMY-1 cells (2.09 ± 0.35 vs. $1.71 \pm 0.10\%$, $p > .05$). As shown in the fluorescence

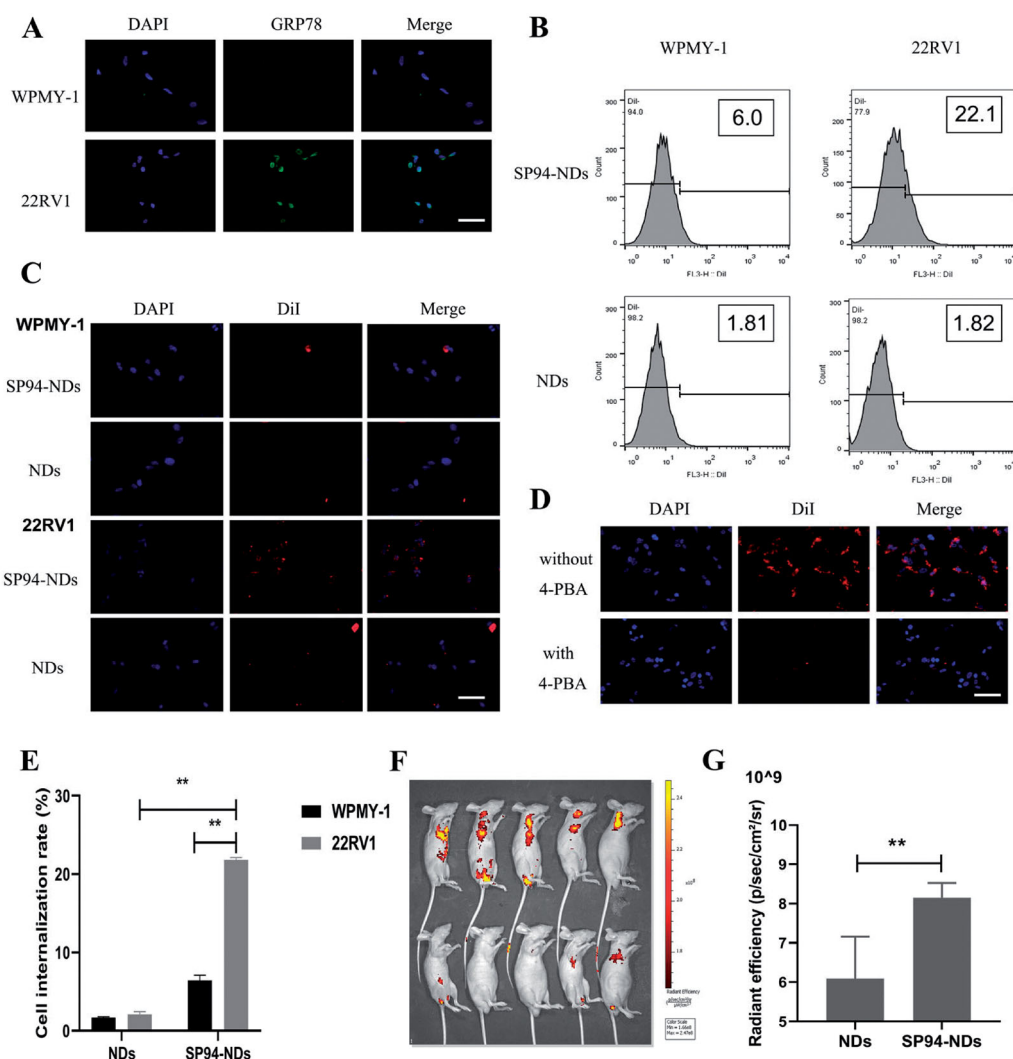


Figure 3. Targeted binding ability. (A) Fluorescence images of WPMY-1 cells and 22RV1 cells incubated with anti-GRP78 antibodies. GRP78 combined with DyLight 488-labeled IgG exhibited green fluorescence, and the nuclei labeled with DAPI staining solution exhibited blue fluorescence. Scale bar: 25 μm . (B) FCM of WPMY-1 cells and 22RV1 cells incubated with targeted SP94-NDs or non-targeted NDs. (C) Fluorescence images of WPMY-1 cells and 22RV1 cells incubated with targeted SP94-NDs or non-targeted NDs. DiI-labeled SP94-NDs and NDs are shown as red dots, while the nuclei labeled with DAPI are shown as blue dots. Scale bar: 25 μm . (D) Fluorescence images of 22RV1 cells pretreated with and without 4-PBA. Scale bar: 25 μm . (E) Quantitative histogram of the FCM result. (F) *In vivo* targeted ability by IVIS. (G) The average intensity of tumors from (F) (** $p < .01$).

images in Figure 3(D), the red fluorescence decreased markedly when pretreated with 4-PBA compared with another group, further suggesting that SP94-NDs could specifically bind to 22RV1 cells expressing GRP78. Figure 3(F) exhibited the *in vivo* targeted ability of the non-targeted NDs and SP94-NDs labeled by the fluorescent molecule DiI. Interestingly, a large number of SP94-NDs gathered in the tumor area, while a small number of non-targeted NDs gathered in the tumor area. The average fluorescence intensity in the tumor area was analyzed statistically (Figure 3(G)), and the SP94-NDs group exhibited a significantly higher intensity than the non-targeted NDs group $[(8.15 \pm 0.37) \times 10^9 \text{ vs. } (6.09 \pm 1.07) \times 10^9, p < .01]$, which could be explained by the enhanced tumor accumulation facilitated by GRP78-mediated targeted delivery.

3.4. CEUI

The CEUI ability was one critical function of SP94-NDs. In Figure 4(A), the SP94-NDs achieved obvious ultrasound

enhancement with PBS as the control. The contrast intensity of SP94-NDs increased markedly from 0 to 3 min and then decreased slowly from 3 to 15 min (Figure 4(B)). The ultrasound signal of the tumor site in a nude mouse became stronger after injection of the SP94-NDs (Figure 4(C)).

3.5. *In vitro* antitumor effect

DOX is commonly used to treat various cancers. To reduce drug toxicity caused by systemic administration, further research is needed to increase the drug concentration at the tumor site. Herein, we prepared targeted ultrasonic nano-droplets for loading DOX. The results regarding optimizing DOX-loaded SP94-NDs are shown in Figures 5(A,B). A concentration of 3 mg/mL was found to be optimal, at which EE (75.5%) and LE (50.4%) were both satisfactory.

DOX inflicted the toxicity of 22RV1 cells in a dose-dependent manner at 24 h, and the IC₅₀ value was 3.6 $\mu\text{g}/\text{mL}$. The results of fluorescence microscopy from Figure 5(D) show

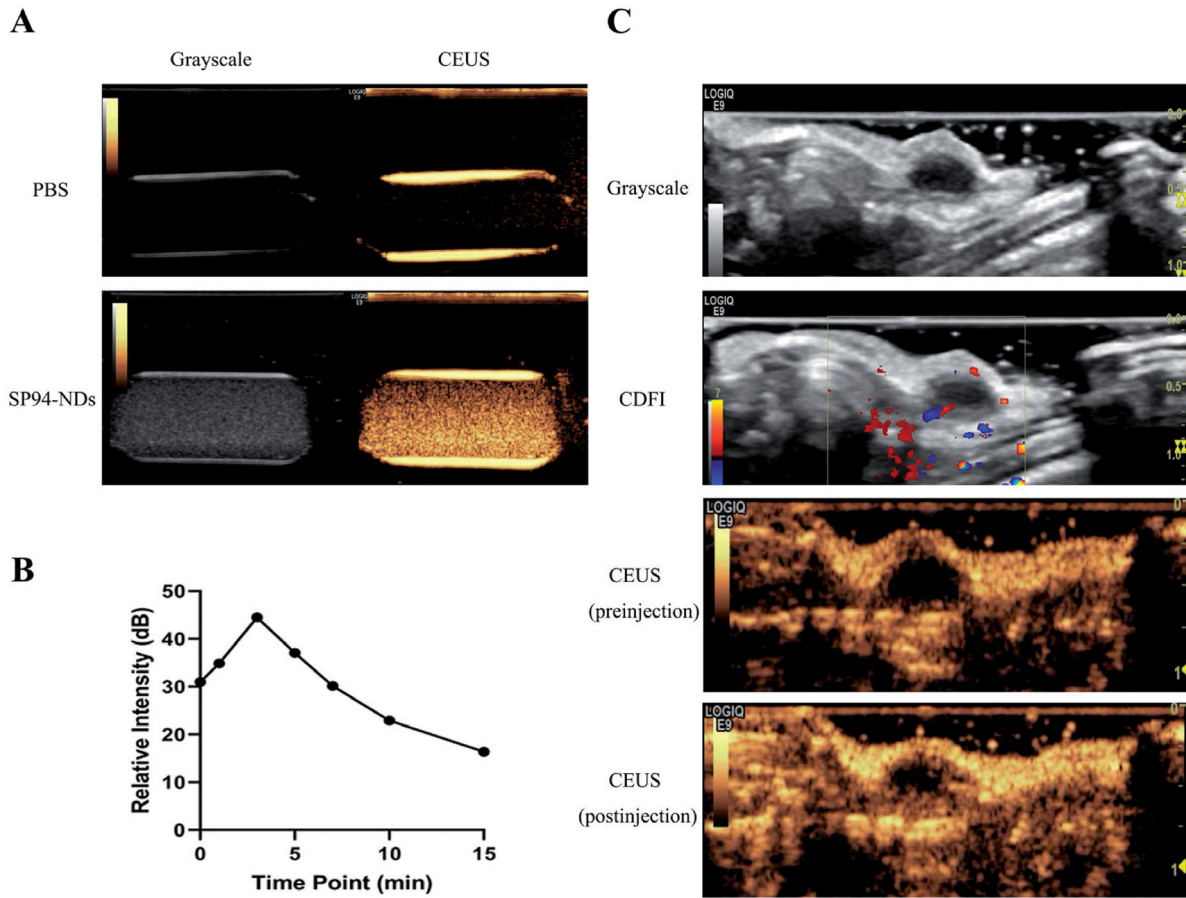


Figure 4. CEUI. (A) Ultrasound images of SP94-NDs *in vitro*. PBS was used as a negative control. (B) Time-intensity curve of SP94-NDs *in vitro* within 15 min. (C) Ultrasound images of SP94-NDs *in vivo*. Data are expressed as means \pm SD ($n = 3$).

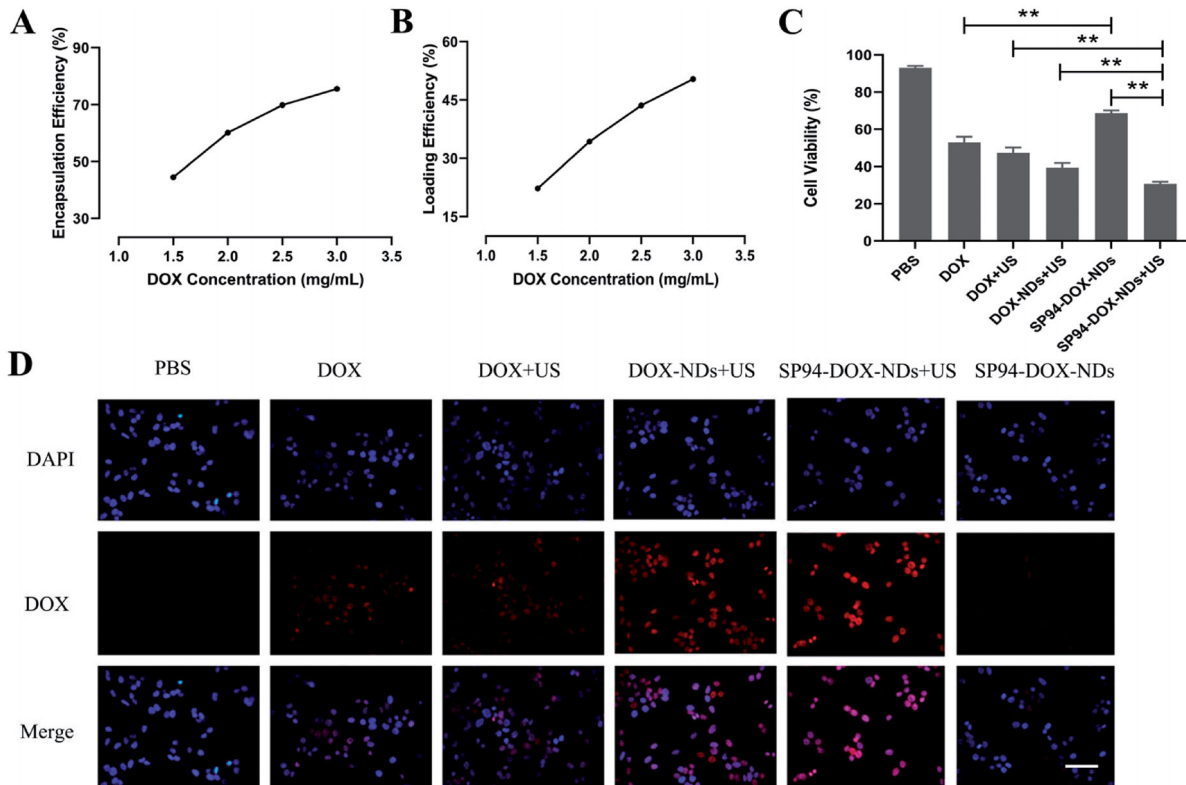


Figure 5. *In vitro* antitumor effect. (A) EE of DOX-loaded SP94-NDs. (B) LE of DOX-loaded SP94-NDs. (C) Cell viability comparison between various groups (** $p < .01$). (D) Intracellular uptake of DOX assessed by fluorescence microscopy. DOX exhibited red fluorescence, and the nuclei labeled with DAPI staining solution exhibited blue fluorescence. Scale bar: 50 μ m. Data are expressed as means \pm SD ($n = 3$).

that intracellular uptake of DOX in various groups was in the order of SP94-DOX-NDs + US > DOX-NDs + US > DOX + US > DOX > SP94-DOX-NDs > PBS control. Also, the antitumor effect in various groups was of the same order, as shown in Figure 5(C). The SP94-DOX-NDs + US group exhibited greater fluorescence intensities than the DOX + US group; thus, the cell viability of the SP94-DOX-NDs + US group ($30.67 \pm 1.16\%$, $p < .01$) was lower than that of the DOX + US group ($47.33 \pm 2.89\%$). In contrast, compared with the free DOX group, the fluorescence intensities were markedly lower in the SP94-DOX-NDs group, whereas the cell viability of the SP94-DOX-NDs group ($68.67 \pm 1.53\%$, $p < .01$) was higher than that of the DOX group ($53.00 \pm 3.00\%$). In addition, the

SP94-DOX-NDs + US group showed more fluorescence than the DOX-NDs + US group. Therefore, the SP94-DOX-NDs + US group ($30.67 \pm 1.16\%$) exhibited lower viability than the DOX-NDs + US group ($39.33 \pm 2.52\%$, $p < .01$). The PBS group displayed no fluorescence; thus, there was no marked cytotoxicity ($93.00 \pm 1.00\%$).

3.6. In vivo antitumor effect

On day 14, the tumors were excised and photographed (Figure 6(A)). No marked difference in body weight was observed among the different groups (Figure 6(C)), indicating

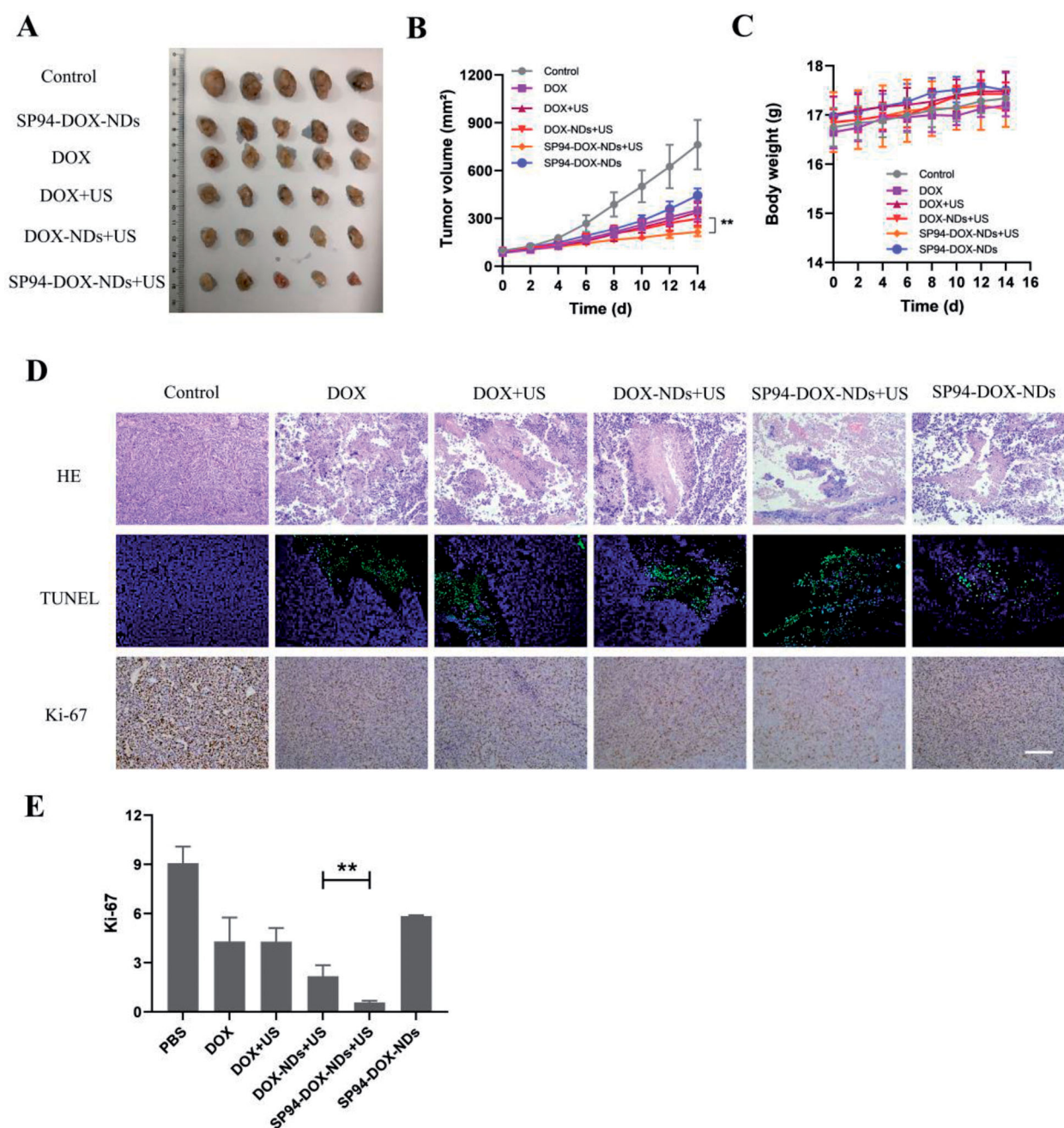


Figure 6. In vivo antitumor effect. (A) Photographs of the tumors removed from the nude mice in different treatment groups. (B) Tumor volume growth (** $p < .01$). (C) Body weight changes of mice. (D) HE, TUNEL, and Ki-67 staining of tumor sections after different treatments. (TUNEL positive: green) (Ki-67 positive: brown). Scale bar: 50 μm . (E) Quantification of brown areas (Ki-67 positive) using ImageJ according to the image in (D) (** $p < .01$). Data are expressed as means \pm SD ($n = 5$).

that there was no systemic toxicity to mice during the treatment. In **Figure 6(B)**, the PBS group exhibited no antitumor effect, and the tumor volume increased from 100 ± 7 to $763 \pm 156 \text{ mm}^3$ at the end of day 14. The tumor volume of DOX ($351 \pm 58 \text{ mm}^3$) was significantly smaller than that of SP94-DOX-NDs ($445 \pm 44 \text{ mm}^3$, $p < .05$). More importantly, the SP94-DOX-NDs + US group exhibited the most significant reduction in tumor volume, and the final mean tumor volume was $215 \pm 28 \text{ mm}^3$, which was evidently smaller than that of the DOX-NDs + US group ($298 \pm 44 \text{ mm}^3$, $p < .01$) and the DOX + US group ($337 \pm 60 \text{ mm}^3$, $p < .01$).

To describe the antitumor effects in more detail, immunohistochemistry and immunofluorescence were performed. **Figure 6(D)** shows tumor slices stained with HE, TUNEL, and Ki-67. Tumors of the PBS group increased vigorously with no marked cell apoptosis, while the SP94-DOX-NDs + US group showed the most apparent damage with a large number of apoptotic cells. In addition, tumors in the PBS group showed large areas of cell proliferation; small areas of proliferation occurred in the SP94-DOX-NDs, DOX, DOX + US, DOX-NDs + US, and SP94-DOX-NDs + US groups, and the smallest occurred in the SP94-DOX-NDs + US group (**Figure 6(E)**), indicating that the antitumor effect was stronger in the SP94-DOX-NDs + US group than in the other groups. These results agree with those of the *in vitro* study.

4. Discussion

In most cases, PCa develops from prostate intraepithelial neoplasia through locally invasive adenocarcinoma to CRPC, which leads to resistance to chemotherapy and radiotherapy and shortens survival time (Nuhn et al., 2019). Thus, it is important to explore a well-tolerated and highly effective treatment. Ultrasonic nanodroplets have become a promising method in modern cancer treatment because they can serve as carriers to deliver drugs and achieve precise tumor treatment. While enhancing the therapeutic effect, ultrasonic nanodroplets can mitigate drug degradation and decrease side effects in normal cells.

For more effective therapy, ultrasonic nanodroplets can be actively targeted at tumor sites. GRP78 is overexpressed in CRPC cells but not in normal prostate cells. We investigated whether SP94-NDs could bind to 22RV1 cells overexpressing GRP78. Innovatively, the SP94 peptide was used as a ligand modified on the surface of ultrasonic nanodroplets to specifically target GRP78 expressed on 22RV1 cells. GRP78 is expressed in CRPC and other cancers, such as lung cancer, colon cancer, and ovarian cancer (Fu & Lee, 2006), which implies that the proposed strategy may apply to other cancers. In addition, the diameter of the SP94-NDs was $\sim 299.7 \text{ nm}$, allowing them to gather in tumors through the EPR effect. Therefore, the fabricated SP94-NDs were expected to passively and actively target tumor tissues, thus decreasing damage to normal tissues (Danquah et al., 2011; Smith et al., 2012).

DOX exhibits a powerful antitumor effect by inhibiting the nucleic acid synthesis in cells; however, direct use of DOX has related toxic effects. It is important to reduce toxic

effects on normal cells and enhance drug concentrations on tumor cells. In this study, we prepared SP94-DOX-NDs to encapsulate DOX. The DOX group exhibited lower cell viability than the SP94-DOX-NDs group, indicating that the SP94-DOX-NDs could protect DOX from being released and thereby ameliorate the systemic toxicity caused by DOX. In addition, we combined ultrasound with SP94-DOX-NDs to enhance the antitumor effect. Experimental results confirmed that the SP94-DOX-NDs + US inhibited tumor growth more significantly than the SP94-DOX-NDs alone. This result suggested that when the nanodroplets were destroyed by the ultrasound, the sonoporation effect improved the permeability of the cell membrane and advanced drug entry into target cells, significantly enhancing the therapeutic effect (Tayier et al., 2019). The results are consistent with those of a previous study: ultrasound induces on-demand drug release in nanodroplets, thus improving the therapeutic effect while decreasing the side effects of the drug on normal tissues (Meng et al., 2019). More importantly, the SP94-DOX-NDs + US group exhibited lower viability than the DOX-NDs + US group, which showed that the modification of SP94 further enhanced the therapeutic ability of drug-loaded nanodroplets. The results in nude mice also showed that the SP94 peptide was beneficial to the accumulation of SP94-DOX-NDs at the tumor site and that SP94-DOX-NDs could locally release DOX under ultrasound irradiation, thereby significantly improving the antitumor effect.

Nanodroplets with a strong contrast-enhanced ultrasound imaging ability and long contrast duration are favorable. The SP94-NDs exhibited enhanced echo signals *in vitro* and *in vivo*. Interestingly, the echo intensity initially increased over time and then slowly decreased, which may be explained by the fact that ultrasound causes the liquid-to-gas transition of nanodroplets to form large microbubbles. Compared with original droplets, large microbubbles were highly echogenic with greater acoustic impedance (Rapoport et al., 2009; Wang et al., 2012; Baghbani et al., 2017).

Based on these results, the newly developed SP94-DOX-NDs could be used as DDSs as well as non-invasive contrast agents, which realized site- and time-specific drug release using ultrasound irradiation in CRPC theranostics. Subsequent research should focus on experiments involving additional cell lines and more diverse ultrasonic nanodroplets.

5. Conclusions

In this study, we successfully fabricated the GRP78-targeted nanodroplets (SP94-DOX-NDs) to serve as a nanoplatform with both highly specific targeting ability for chemotherapy and ultrasound imaging capability. First, the GRP78-targeted nanodroplets enhanced the targeting ability to CRPC. Second, the GRP78-targeted nanodroplets were found to be able to release drugs at specific times and positions and enhance drug uptake through ultrasound sonoporation. Third, the GRP78-targeted nanodroplets could be used as an ultrasound contrast enhancer. Considering all of the results in this study, we designed novel oncotherapy nanodroplets that combined imaging diagnosis and high therapeutic

performance, which provides an innovative method for precise cancer treatment.

Disclosure statement

The authors declare no conflicts of interest in this study.

Funding

This study was supported by the National Natural Science Foundation of China (Nos. 81771843 and 82071937) and Shandong Provincial Natural Science Foundation, China (No. ZR2019PH067).

ORCID

Yading Zhao  <http://orcid.org/0000-0001-6607-8597>

Xiaoying Zhou  <http://orcid.org/0000-0002-8329-4707>

Data availability statement

The data used to support the findings of this study are available from the corresponding author upon reasonable request.

References

- Baghbani F, Chegeni M, Moztaaradeh F, et al. (2017). Novel ultrasound-responsive chitosan/perfluorohexane nanodroplets for image-guided smart delivery of an anticancer agent: curcumin. *Mater Sci Eng C Mater Biol Appl* 74:186–93.
- Baghbani F, Moztaaradeh F, Mohandesi JA, et al. (2016). Formulation design, preparation and characterization of multifunctional alginate stabilized nanodroplets. *Int J Biol Macromol* 89:550–8.
- Bray F, Ferlay J, Soerjomataram I, et al. (2018). Global cancer statistics 2018: GLOBOCAN estimates of incidence and mortality worldwide for 36 cancers in 185 countries. *CA Cancer J Clin* 68:394–424.
- Cai L, Wang X, Wang W, et al. (2012). Peptide ligand and PEG-mediated long-circulating liposome targeted to FGFR overexpressing tumor *in vivo*. *Int J Nanomedicine* 7:4499–510.
- Chen J, Lin Z, Deng K, et al. (2019). Tension induces intervertebral disc degeneration via endoplasmic reticulum stress-mediated autophagy. *Biosci Rep* 39:BSR20190578.
- Danquah MK, Zhang XA, Mahato RI. (2011). Extravasation of polymeric nanomedicines across tumor vasculature. *Adv Drug Deliv Rev* 63: 623–39.
- Delie F, Petignat P, Cohen M. (2013). GRP78-targeted nanotherapy against castrate-resistant prostate cancer cells expressing membrane GRP78. *Target Oncol* 8:225–30.
- Du YZ, Cai LL, Liu P, et al. (2012). Tumor cells-specific targeting delivery achieved by A54 peptide functionalized polymeric micelles. *Biomaterials* 33:8858–67.
- Duan S, Guo L, Shi D, et al. (2017). Development of a novel folate-modified nanobubbles with improved targeting ability to tumor cells. *Ultrason Sonochem* 37:235–43.
- Fu Y, Lee AS. (2006). Glucose regulated proteins in cancer progression, drug resistance and immunotherapy. *Cancer Biol Ther* 5:741–4.
- Jiang B, Zhang R, Zhang J, et al. (2019). GRP78-targeted ferritin nanocaged ultra-high dose of doxorubicin for hepatocellular carcinoma therapy. *Theranostics* 9:2167–82.
- Jiang C, Zhang S, Li D, et al. (2020). Impaired ferritinophagy flux induced by high fat diet mediates hepatic insulin resistance via endoplasmic reticulum stress. *Food Chem Toxicol* 140:111329.
- Kripfgans OD, Fabiilli ML, Carson PL, Fowlkes JB. (2004). On the acoustic vaporization of micrometer-sized droplets. *J Acoust Soc Am* 116: 272–81.
- Lee AS. (2007). GRP78 induction in cancer: therapeutic and prognostic implications. *Cancer Res* 67:3496–9.
- Lee AS. (2014). Glucose-regulated proteins in cancer: molecular mechanisms and therapeutic potential. *Nat Rev Cancer* 14:263–76.
- Lekshmi U, Kishore N, Reddy P. (2011). Sub acute toxicity assessment of glipizide engineered polymeric nanoparticles. *J Biomed Nanotechnol* 2017:2578–89.
- Li DS, Jeng G-S, Pitre JJ, et al. (2020). Spatially localized sono-photoacoustic activation of phase-change contrast agents. *Photoacoustics* 20:100202.
- Li X, Yang X, Lin Z, et al. (2015). A folate modified pH sensitive targeted polymeric micelle alleviated systemic toxicity of doxorubicin (DOX) in multi-drug resistant tumor bearing mice. *Eur J Pharm Sci* 76: 95–101.
- Lv Y, Cao Y, Li P, et al. (2017). Ultrasound-triggered destruction of folate-functionalized mesoporous silica nanoparticle-loaded microbubble for targeted tumor therapy. *Adv Healthcare Mater* 6:1700354.
- Meng D, Guo L, Shi D, et al. (2019). Charge-conversion and ultrasound-responsive O-carboxymethyl chitosan nanodroplets for controlled drug delivery. *Nanomedicine* 14:2549–65.
- Nuhn P, Bono J, Fizazi K, et al. (2019). Update on systemic prostate cancer therapies: management of metastatic castration-resistant prostate cancer in the era of precision oncology. *Eur Urol* 75:88–99.
- Pootrakul L, Datar RH, Shi SR, et al. (2006). Expression of stress response protein Grp78 is associated with the development of castration-resistant prostate cancer. *Clin Cancer Res* 12:5987–93.
- Rapoport NY, Kennedy AM, Shea JE, et al. (2009). Controlled and targeted tumor chemotherapy by ultrasound-activated nanoemulsions/microbubbles. *J Control Release* 138:268–76.
- Schottelius M, Wester H-J. (2009). Molecular imaging targeting peptide receptors. *Methods* 48:161–77.
- Smith BR, Kempen P, Bouley D, et al. (2012). Shape matters: intravital microscopy reveals surprising geometrical dependence for nanoparticles in tumor models of extravasation. *Nano Lett* 12:3369–77.
- Tayier B, Deng Z, Wang Y, et al. (2019). Biosynthetic nanobubbles for targeted gene delivery by focused ultrasound. *Nanoscale* 11:14757–68.
- Wang C, Kang S, Lee Y, et al. (2012). Aptamer-conjugated and drug-loaded acoustic droplets for ultrasound theranosis. *Biomaterials* 33: 1939–47.
- Yang H, Cai W, Xu L, et al. (2015). Nanobubble-Affibody: novel ultrasound contrast agents for targeted molecular ultrasound imaging of tumor. *Biomaterials* 37:279–88.
- Zhang Y, Liu R, Ni M, et al. (2010). Cell surface relocalization of the endoplasmic reticulum chaperone and unfolded protein response regulator GRP78/BiP. *J Biol Chem* 285:15065–75.